Supplement of Atmos. Chem. Phys., 22, 7933–7958, 2022
https://doi.org/10.5194/acp-22-7933-2022-supplement

Atmospheric Chemistry and Physics
Open Access

Supplement of

Limitations in representation of physical processes prevent successful simulation of $PM_{2.5}$ during KORUS-AQ

Katherine R. Travis et al.

Correspondence to: Katherine R. Travis (katherine.travis@nasa.gov)

Table S1 - Translation of KORUSv5 emissions inventory to GEOS-Chem mechanism[1]

SAPRC99	# Carbons in SAPRC99	GEOS-Chem[2]	# Carbons in GEOS-Chem	Scale factor[4]
NO	N/A	NO	N/A	1
NO2	N/A	NO2	N/A	1
CO	1	CO	1	1
HCHO	1	CH2O	1	1
MEOH	1	MOH	1	1
MVK	4	MVK	4	1
MGLY	3	MGLY	3	1
MEK	4	MEK	4	1
PRD2	6	MEK	4	6/4
MACR	4	MACR	4	1
ISOP	5	ISOP	5	1
ETHE	2	C2H4	2	1
GLY	2	GLYX	2	1
BACL	4	BACL	4	1
ACET	3	ACET	3	1
CRES	7	CRES	7	1
BALD	7	BALD	7	1
PHEN	6	PHEN	6	1
RCHO	3	RCHO	3	1
SO2	N/A	SO2	N/A	1
SULF	N/A	SO2	N/A	1
NH3	N/A	NH3	N/A	1
ALK1	2	C2H6	2	1
ALK2	3	C3H8	3	1
ALK3	4	ALK4	4.3	4/4.3
ALK4	5	ALK4	4.3	5/4.3
ALK5	8	ALK4	4.3	8/4.3
OLE1	5	PRPE	3	5/3
OLE2	5	PRPE	3	5/3

SAPRC99	# Carbons in SAPRC99	GEOS-Chem[2]	# Carbons in GEOS-Chem	Scale factor[4]
CCHO	2	ALD2	2	1
IPRD	5	IPRD	5	1
TERP	10	MTPA	10	1
PSO4	N/A	SO4	N/A	1
ARO1	7	BENZ	6	0.1[3]
ARO1	9	TOLU	7	0.9[3]
ARO2	9	XYLE	8	9/8
PEC	1	BC	1	1
PNO3	N/A	NIT	N/A	1
HCOOH	1	HCOOH	1	1

[1]Model translation of KORUSv5 emissions inventory based on these documents - http://citeseerx.ist.psu.edu/viewdoc/download?doi=10.1.1.25.293&rep=rep1&type=pdf https://www.atmos-chem-phys.net/14/5617/2014/acp-14-5617-2014.pdf

[2]GEOS-Chem species definitions are provided here: http://wiki.seas.harvard.edu/geos-chem/index.php/Species_in_GEOS-Chem

[3]Pers. Communication, Isobel Simpson

[4]Conversion from SAPRC99 species carbon number to GEOS-Chem species carbon number

Table S2 - Halogen heterogeneous reactions leading to the formation of HNO_3[1]

$BrNO_3 + H2O = HOBr + HNO_3$
$BrNO_3 + HCl = BrCl + HNO_3$
$ClNO_3 + H2O = HOCl + HNO_3$
$ClNO_3 + HCl = Cl_2 + HNO_3$
$ClNO_3 + HBr = BrCl + HNO_3$
$ClNO_3 + BrSALA = BrCl + HNO_3$
$ClNO_3 + BrSALC = BrCl + HNO_3$
$ClNO_3 + BrSALC = BrCl + HNO_3$
$IONO_2 = 0.85ICl + 0.15IBr + HNO_3$

[1]GEOS-Chem species definitions are provided here: http://wiki.seas.harvard.edu/geos-chem/index.php/Species_in_GEOS-Chem

S1 Impact of dust on $PM_{2.5}$ during KORUS-AQ

Significant dust concentrations, which could degrade the use of PM_1 to interpret $PM_{2.5}$, were observed at surface sites during the first part of the campaign (before May 9th), as discussed in Heim et al. (2020). Figure S1 shows the divergence of PM_{10} from $PM_{2.5}$ at Olympic Park (a) and across Seoul (b) before May 9th while during the rest of the campaign they are highly correlated confirming the lack of surface dust influence after this period. We exclude dust from our analysis of $PM_{2.5}$ composition and assume that PM_1 composition can be used to investigate the drivers of $PM_{2.5}$ pollution during the different meteorological periods of the campaign. Dust was similarly unimportant to $PM_{2.5}$ levels during a haze event analyzed using speciated PM_1 and $PM_{2.5}$ observations in Seoul in March 2019 (Schlosser et al., 2022).

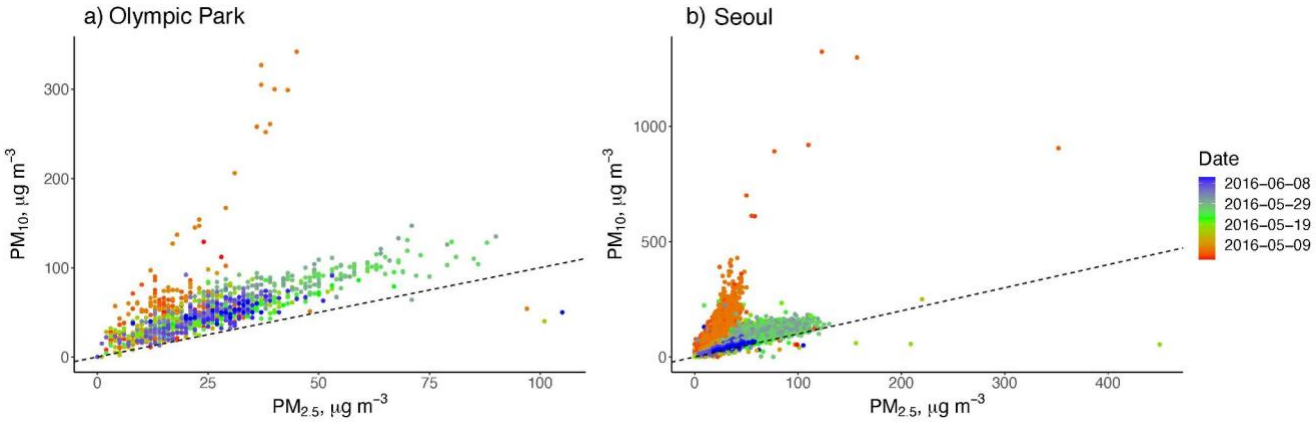

Figure S1. $PM_{2.5}$ vs. PM_{10} at the Olympic Park AirKorea site (b) and for the Seoul Region (b). The dashed line indicates the 1-1 line.

S2 Speciation of observed $PM_{2.5}$ mass using PM_1 composition

Measured composition from the KIST HR-ToF-AMS instrument (Table 1), representative of PM_1 (Guo et al., 2021), is used to speciate daily average $PM_{2.5}$ from the AirKorea sites (Fig. 1a). Jordan et al. (2020) showed that speciated PM_1 was generally representative of $PM_{2.5}$ mass throughout KORUS-AQ, except for the Transport/Haze period when $PM_{2.5}$ exceeded PM_1. The strong correlation between $PM_{2.5}$ and PM_1 during the campaign implied growth of PM_1 to larger sizes. Dust is not a major component of $PM_{2.5}$ at the surface after May 9th, as further discussed in Section S1. Therefore, PM_1 composition likely represents the composition of $PM_{2.5}$ with the exception of a small contribution from primary aerosol species. This was shown to be true in Seoul using speciated PM_1 and $PM_{2.5}$ observations in March 2019 (Schlosser et al., 2022). Sun et al. (2020) showed that $PM_{2.5}$ can be up to 50% greater than PM_1 in polluted, humid environments due to growth of secondary species (not BC or POA). We remove BC and POA from observed $PM_{2.5}$ and scale the remaining components (SNA, SOA) to the remaining $PM_{2.5}$.

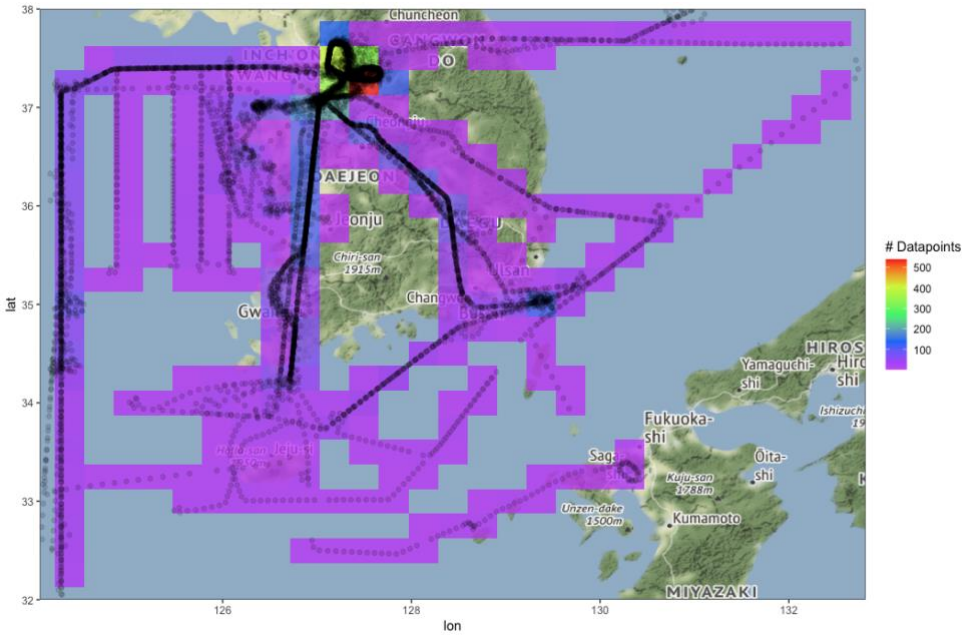

Figure S2. Data density of flight tracks in each GEOS-Chem grid box in the study domain. Map tiles by Stamen Design , under CC BY 3.0. Data by OpenStreetMap, under ODbL.

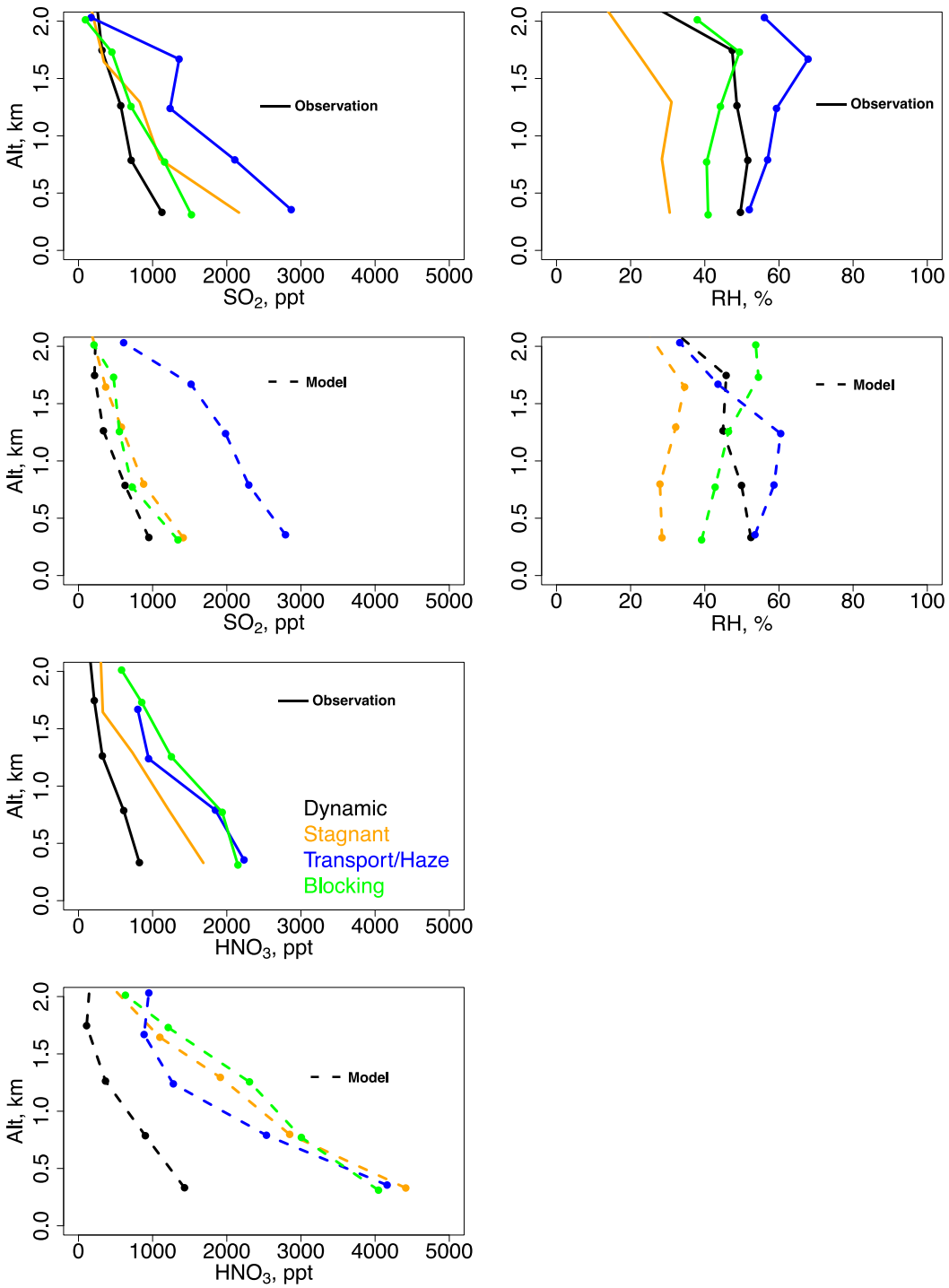

Figure S3. The same as Fig. 3 for SO_2, HNO_3, and relative humidity.

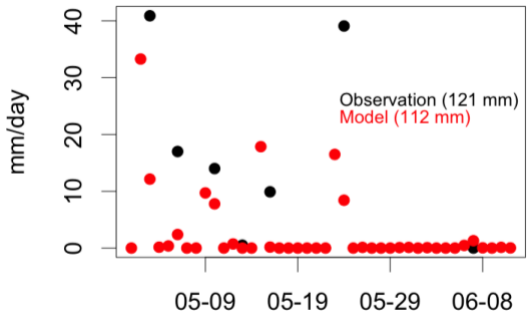

Figure S4. Daily precipitation for 2016 in Seoul from https://www.ncdc.noaa.gov/cdo-web/datasets.

S3 Discussion of HNO_3 loss pathways

The revised GEOS-Chem wet scavenging scheme improved annual average simulations of HNO_3 concentrations by 50% (Luo et al., 2019). Figure 4b shows the impact of reverting to the old wet scavenging scheme on model HNO_3, where the new scheme results in reduced daytime (nighttime) nitric acid of -330 ppt (-100 ppt) or 12% in the daily average. This reduction is less than the result from Luo et al. (2019), which we attribute to the lower amount of precipitation during May-June in this region than on an annual average. Along the flight tracks (Fig. 6), HNO_3 decreases by only ~8% below 0.5 km. This reflects both the sampling bias towards clear-sky conditions in the aircraft observations and the larger impact of the revised wet scavenging on washout (below-cloud scavenging), which impacts surface concentrations, compared to rainout (in-cloud scavenging), that has a larger impact on concentrations aloft. Figure 4a shows that the daily average reduction in nitrate (-38%) is approximately three times greater than that of HNO_3 (-12%), likely due to the longer nitrate lifetime against dry deposition (~1 week) compared to HNO_3 (<2 days) allowing for infrequent precipitation to have a larger impact. This rapid loss to deposition suggests that the model bias in HNO_3, present during most of the campaign, cannot be resolved by wet scavenging.

Other loss pathways for HNO_3, such as uptake to dust (Fairlie et al., 2010), are not expected to play a large role during KORUS-AQ as dust concentrations were low after the first week of the campaign (Heim et al., 2020). We calculate 10% of average nitrate below 0.5 km across all periods of the campaign (Fig. 3, 0.8 μg m^{-3}) to be equivalent to approximately ~270 ppt of HNO_3, or <20% of the model bias. In certain locations around the world, seasalt uptake of HNO_3 may be another pathway to reduce model HNO_3 biases (Wang et al., 2019). This uptake results in displacement of HCl that is transported inland and participates in R2 to produce $ClNO_2$. We estimate the potential for seasalt to reduce model HNO_3 levels by determining the observed excess Na^+ available to form $NaNO_3$ by subtracting the available Cl^- to form NaCl (Fig. S5). The excess Na^+ below 0.5 km is 0.001 μmol m^{-3} or 0.03 μg m^{-3}. This corresponds to an associated mixing ratio of HNO_3 of only 30 ppt. Therefore, seasalt uptake of HNO_3 would be expected to have a negligible impact on the model bias. We test a recent model version (12.9.3, doi:10.5281/zenodo.3959279) unavailable at the time of our original study that includes seasalt (Wang et al., 2021) and dust uptake of acids (Fairlie et al., 2010). Figure S6 confirms the negligible effect that dust and seasalt uptake HNO_3 has on the model bias.

Studies have hypothesized that production of $ClNO_2$ from N_2O_5 hydrolysis (R2) could reduce nitrate by decreasing the yield of HNO_3 (Sarwar et al., 2012; Qiu et al., 2019). During KORUS-AQ, high levels of $ClNO_2$ were observed at Olympic Park in the early part of the night (Jeong et al., 2019). We use the model version described above (12.9.3) that includes an observationally-constrained mechanism for $ClNO_2$ production on SNA (R2), OA, and seasalt (Wang et al., 2020) to test the impact of production of $ClNO_2$ on the model nitrate bias. Figure S7 shows that nighttime nitrate is reduced when $ClNO_2$ is in best agreement with the observations (early morning hours). However, the model is missing the early nighttime $ClNO_2$ peak also described by Jeong et al. (2019). This peak supports the finding from Jordan et al. (2020) that N_2O_5 hydrolysis should be rapid throughout the campaign. Therefore, the impact of $ClNO_2$

production could be somewhat larger if the model successfully represented the importance of R2 (N_2O_5 hydrolysis) over R4 (NO_2 uptake, Fig. 5c). We discuss the reasons for the errors in model nighttime production pathway in Section 5.3 (main text).

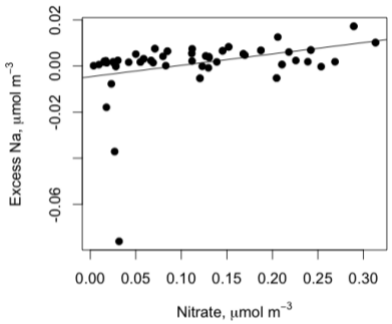

Figure S5. Excess Na^+ calculated as described in Section 5.2 for the domain of Fig. 3 below 0.5 km.

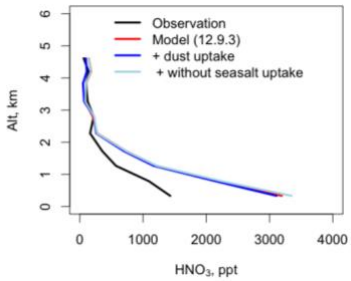

Figure S6. Mean vertical profile of observed and modeled nitric acid as described in Section 5.2 for the same domain as Fig. 3.

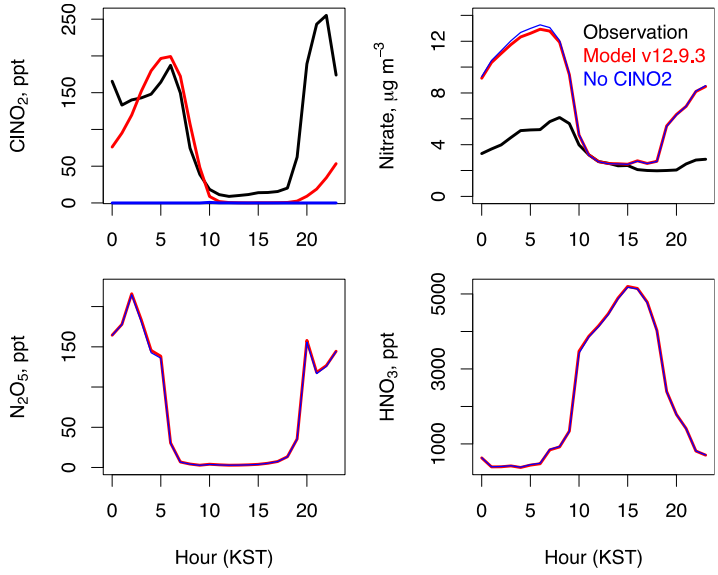

Figure S7. Mean diurnal cycle of modeled and observed $ClNO_2$, nitrate (KIST), and modeled N_2O_5 and HNO_3. The sensitivity studies are described in Section 5.2 and Section S3 above.

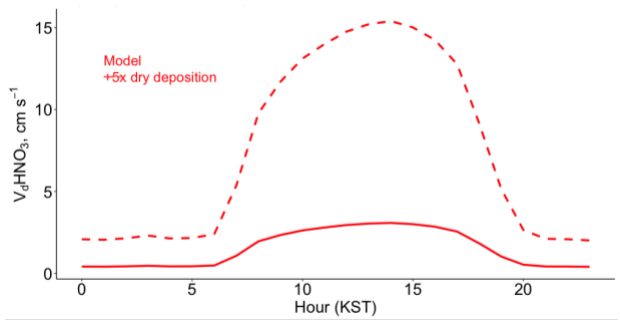

Figure S8. Mean diurnal cycle of model dry deposition velocity (Vd_{HNO3}) from May 1 to June 7, 2016. The sensitivity test is described in Section 5.2.

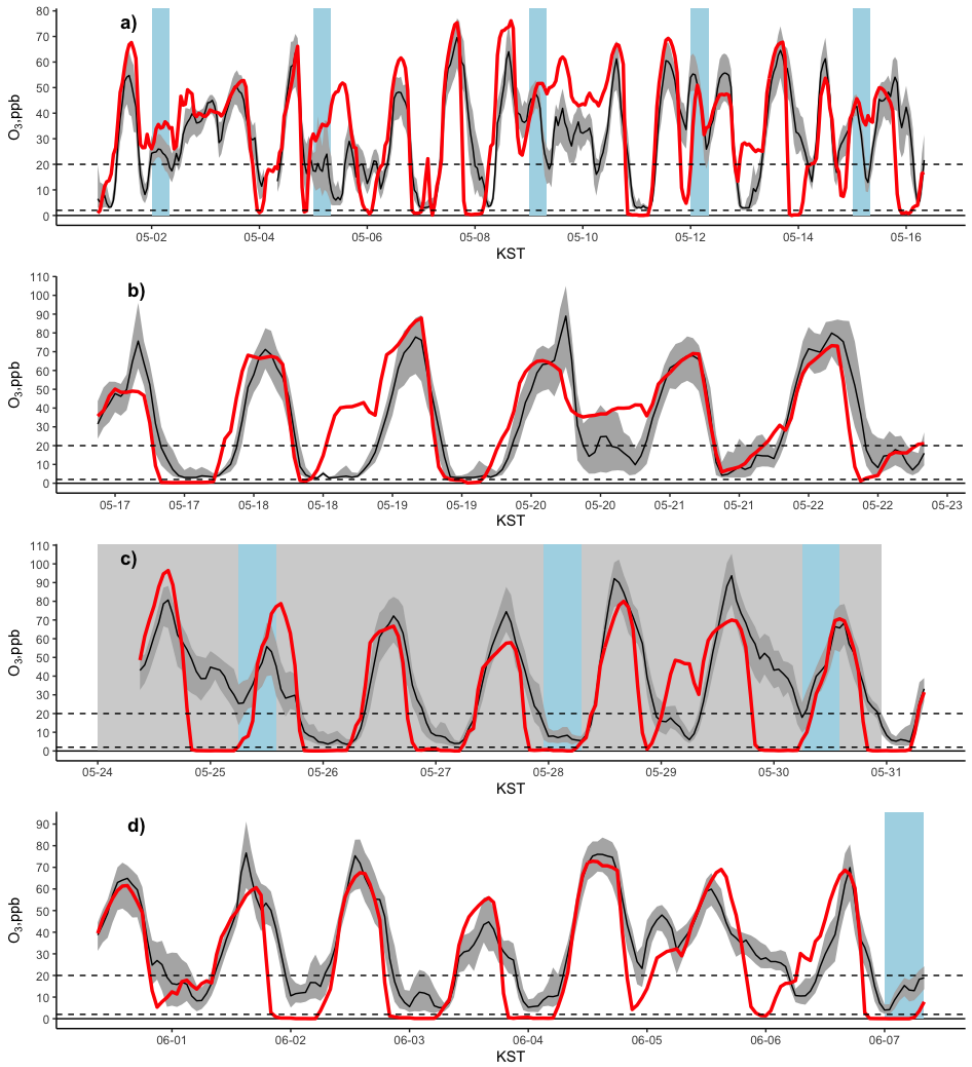

Figure S**9**. Hourly timeseries of ozone for the a) Dynamic, b) Stagnant, c) Transport/Haze, and d) Blocking Periods at the AirKorea sites in the gridbox (Fig. 1b). The median value (black) and interquantile range (grey) are compared against the model (red) for the campaign period. The beginning of frontal passes is shown in blue, and the Transport/Haze Period is highlighted in grey. The dashed lines indicate 20 ppb and 2 ppb.

S4 Calculation of TNO_3 deposition velocity from aircraft

To estimate the HNO_3 deposition velocity, a similar approach was taken as described by Neuman et al. (2004). However, as plume sampling was not part of the flight strategy in the SMA (described in Section 4), the approach to investigate production and losses were similar to Nault et al. (2018). We calculate atmospheric loss for NO_x (to determine its lifetime against conversion to total nitrate, ($TNO_3 = HNO_3 + pNO_3$) and binned observations of TNO_3 as well as total peroxy nitrates (ΣPNs) and the sum of alkyl- and multi-functional nitrates (ΣANs). We calculate photochemical age in a similar manner as in Perring et al. (2010). However, instead of n-butane and 2-butyl nitrate, we use propene and propene hydroxynitrate as propene has a higher rate constant to better capture the rapid photochemistry occurring in SMA (Parrish et al. 2007) and propene was co-emitted with NO_x from transportation sources (Simpson et al. 2020).

The following equation relates the production of propene hydroxynitrate from propene to photochemical age:

$$t = \frac{\ln\left(1 - \frac{[\mathrm{RONO_2}]}{[\mathrm{RH}]}\frac{(k_B - k_A)}{\alpha k_A}\right)}{(k_A - k_B)} \quad \text{Eq. S1}$$

Here, $[RONO_2]$ is the mixing ratio of the propene hydroxynitrate at photochemical time, *t*, [RH] is the mixing ratio of propene at time, *t*, k_B is the loss rate for hydroxynitrate, k_A is the loss rate for propene, and α is the nitrate branching ratio. For α, we use the value of 0.041 from Teng et al. (2015). For k_A, the pressure and temperature dependent rate constant for OH + propene is from Atkinson et al. (2006) along with the average [OH] measured over SMA. For k_B, the rate constant 1×10^{-12} cm^3 $molec.^{-1}$ s^{-1} for OH + propene hydroxynitrate (Saunders et al. 2003; Jenkin et al. 1997) along with [OH] measured over SMA and an assumed photolysis rate constant of $\sim1\times10^{-6}$ s^{-1} (Perring et al. 2010).

For all calculations, we use an average OH across the SMA of 5.2×10^6 molec cm^{-3} at an average temperature of 290.6 K and 1 atm. The NO_x first order lifetime was derived by fitting a least-orthogonal-distance exponential fit to the ratio $\Delta NO_x/\Delta CO$ shown in Fig. 8. TNO_3 vs. photochemical age was fit using Eq. 3, where β was the unknown as a function of photochemical age, and c (= $pTNO_3 = pHNO_3 = k_{R1}[OH]$) is a constant 0.21 hr^{-1} using the SMA average OH.

S5 Weather Sonde Description and Mixed Layer Height Estimation

The weather sondes used are launched regularly at 00:00, 06:00, 12:00, and 18:00 UTC (+9 KST) at the Osan Air Force Base, located in Pyeongtaek, South Korea, (station #47122). The sondes launched between May 1 and June 10, 2016 were used in the analysis. All sondes launched at the same time were combined, and the median values were used for the profiles shown in Figure S10. The Richardson's Number was derived using the following equation,

$$R_{ib}(z) = \frac{g(z - z_0)(\theta(z) - \theta_z)}{\theta(z)\left(u(z)^2 + v(z)^2\right)} \quad \text{Eq. S2}$$

where *g* is the acceleration due to gravity, z_0 is the initial height of the sonde upon launch above sea level, *z* is the measurement altitude above sea level, θ is the potential temperature, and *u(z)* and *v(z)* are the zonal and meridional wind components, respectively. Richardson's number of 0.21 was used to define mixed layer height (MLH). Richardson's number can be subject to uncertainty for conditions of general stagnant conditions, e.g., nighttime.

To further evaluate the value and potential uncertainty associated with estimating the MLH with the Richardson's number, profiles of relative humidity (RH), ambient temperature, and potential temperature were also investigated (Figure S10). Potential temperature is most appropriate for estimating daytime MLH while ambient temperature and

RH can be used to verify potential temperature and Richardson's number. For the potential temperature, the MLH was estimated at the altitude where the potential temperature equaled the potential temperature at the lowest altitude (291 K for 00:00 UTC/09:00 KST and 298 K for 06:00 UTC/15:00 KST). For ambient temperature, the MLH is estimated as the height of the temperature inversion (see Table S4). For RH, the altitude was selected either where RH at altitude equaled the RH at lowest altitude (06:00 UTC/15:00 KST), the altitude where RH remained constant with height before decreasing (00:00 UTC/09:00 KST and 12:00 UTC/21:00 KST), or the altitude that showed lower decrease of RH with altitude after a rapid decrease in altitude (18:00 UTC/03:00 KST) (see Table S4).

The estimated MLH from the median profiles in Figure S10 for each launch time during KORUS-AQ is summarized in Table S4. For the mid-morning and mid-evening (09:00 and 21:00 KST) sondes, the estimated MLH from Richardson's number and either RH and/or air temperature agree within 10%. Larger variability is observed during the time period of most mixing (15:00 KST) and least mixing (03:00 KST). The disagreement between the derived MLH at 03:00 KST is not surprising, as discussed above. Due to the uncertainty in the Richardson's number/MLH at 03:00 KST, the MLH derived from RH and air temperature represent a more realistic value.

Table S3. Estimated boundary layer height (m) from weather sondes launched between May 1 and June 10, 2016 at Osan Air Force Base (Pyeongtaek, South Korea, station #47122) for 00:00 (09:00), 06:00 (15:00), 12:00 (21:00), and 18:00 (03:00) UTC (KST).

Time	Richardson's Number	Relative Humidity	Air Temperature or Potential Temperature
09:00 KST	467	466	466
15:00 KST	1266	1743	1404
21:00 KST	339	325	Not Defined
03:00 KST	119	282	282

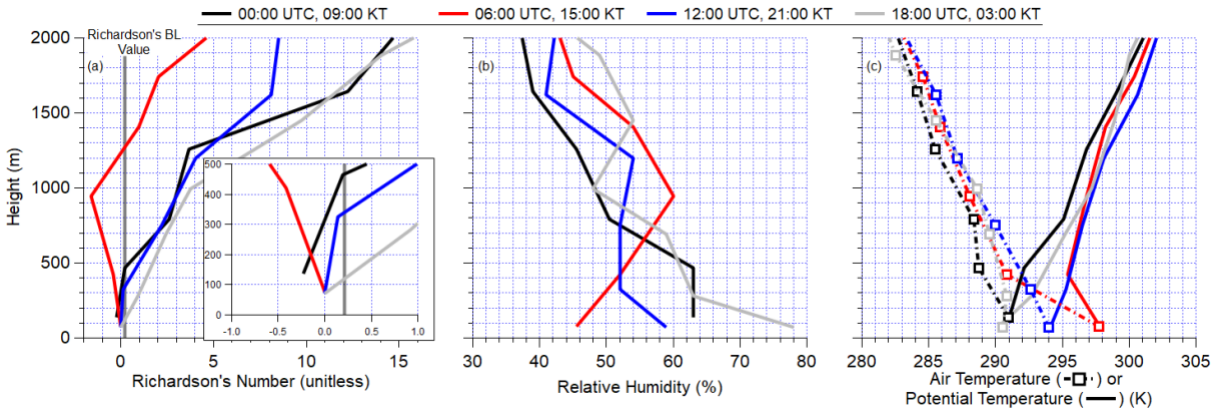

Figure S10. Median profiles of (a) Richardson's Number, (b) Relative Humidity, and (c) Air Temperature and Potential Temperature, for weather sondes launched between 01-May-2021 and 10-June-2021 at at Osan Air Force Base (Pyeongtaek, South Korea, station #47122) for 00:00 (black), 06:00 (red), 12:00 (blue), and 18:00 (grey) UTC. The vertical line in (a) shows the Richardson's Number limit for the MLH (~0.2) (Fairall et al. 2006).

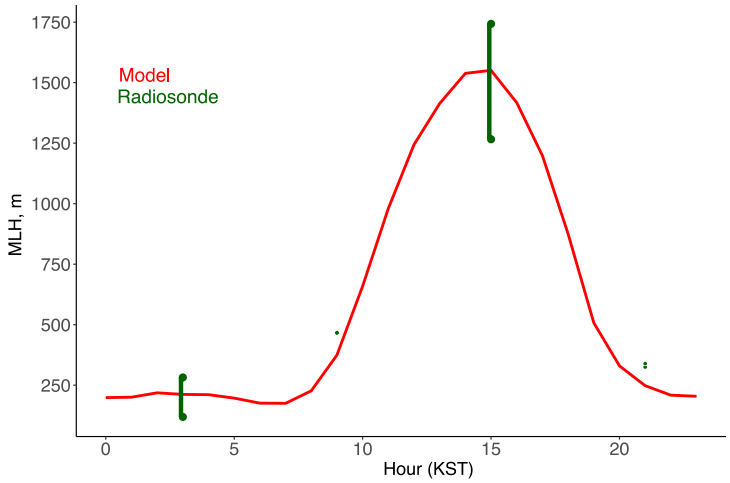

Figure S11. Mean diurnal cycle for the mixed layer height (MLH) from the model at Osan Air Force base compared against the values derived in Table S4.

Section S6 Impact of adjustments to mixed layer height and minimum eddy diffusivity on ozone diurnal cycle

The increase in nighttime mixing in urban vs. rural regions has been addressed in the CMAQ model (Li and Rappenglueck, 2018) by using a higher value for the minimum mixing strength (eddy diffusivity) over urban areas. However, we find that this approach is insufficient to address model ozone titration without increasing the sensible heat flux to a positive value to produce an unstable mixed layer. This is illustrated in Fig. S12, where we scale the model MLH to match the profile at Olympic Park (Fig. 10a) and raise the model minimum eddy diffusivity from 0.01 $m^2\ s^{-1}$ to 1 $m^2\ s^{-1}$ over the SMA. Reducing the collapse of the evening MLH without a change to the drivers of mixing (i.e., heat fluxes, friction velocity) has negligible impact on decreasing model ozone titration (Fig. S12b). In addition, the MLH at Olympic Park in the early morning hours appears inconsistent with observed ozone, likely due to the uncertainties in the measurement technique discussed above and supported by the lower values obtained from radiosonde profiles (Fig. S11).

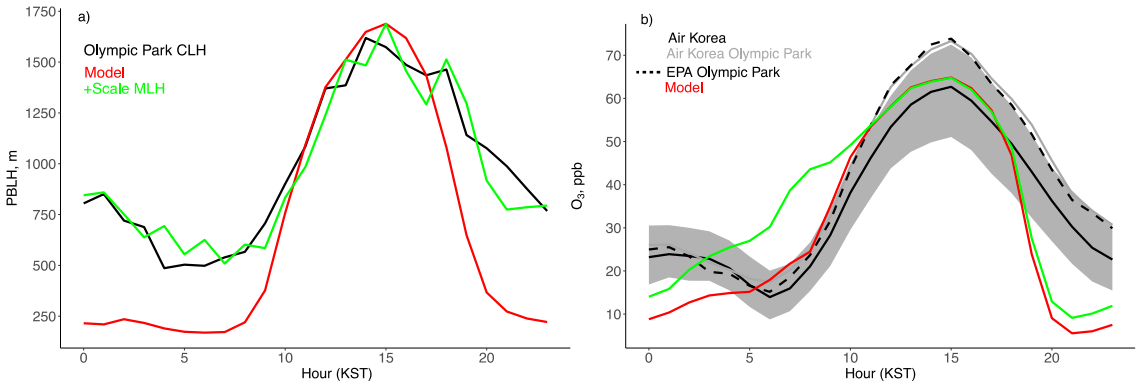

Figure S12. The same as Fig. 10a and 9a but including the sensitivity study described in Section S6. The observations are described in Table 1.

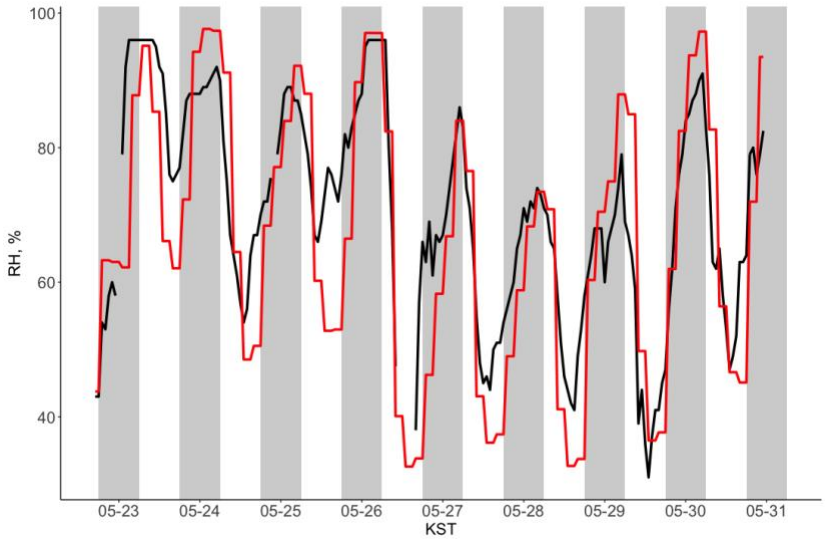

Figure S13. Relative humidity during the Transport/Haze period at Olympic Park from the observations (black) compared against the model (red). The grey shading indicates 6pm to 6am.

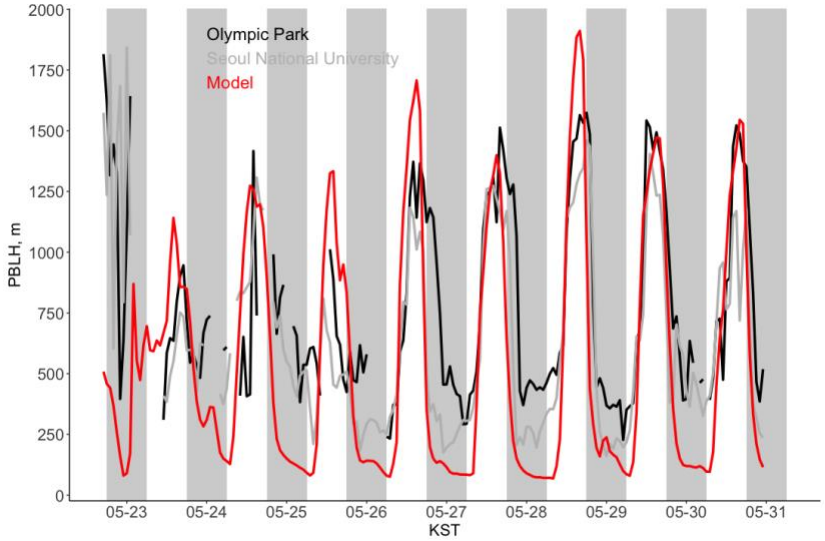

Figure S14. Boundary layer height (PBLH) during the Transport/Haze period from the Olympic Park CLH (black), SNU CLH (grey), and model (red). The grey shading indicates 6pm to 6am.

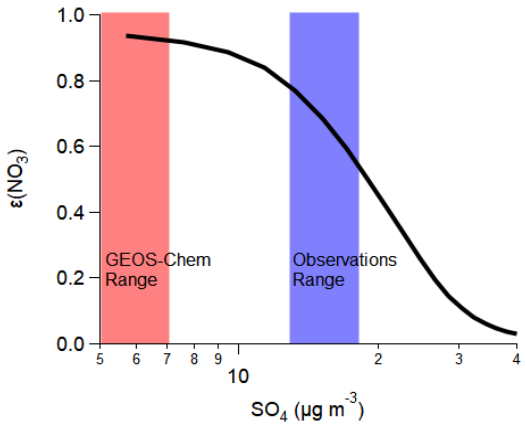

Figure S15. Fraction of particle nitrate (NO_3) to total nitrate (gas- and particle-phase, HNO_3 and NO_3) ($\varepsilon(NO_3)$) versus sulfate (SO_4), from a model run using E-AIM IV. Input into the model was the average meteorological conditions (RH = 80%, T = 288 K) and average nitrate (16 μg m^{-3}), ammonium (8 μg m^{-3}), nitric acid (1800 pptv), and ammonia (3000 pptv) during the transport/haze event. Sulfate varied between ~5 to 100 μg m^{-3}. The results from the E-AIM model are shown as the black line, and the average values from GEOS-Chem and observations during the haze event are highlighted for comparison.

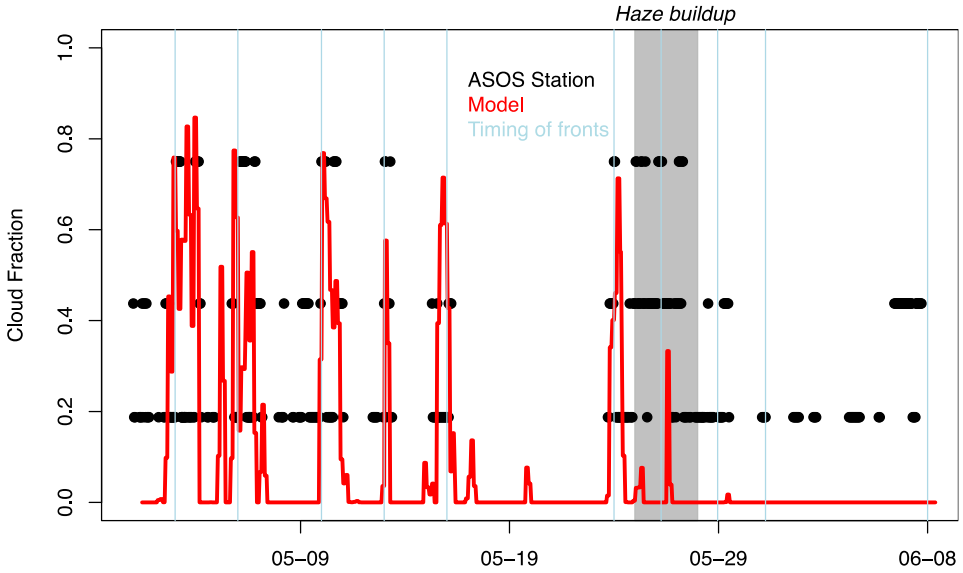

Figure S16. Low cloud fraction (>680 hPa) from the nearest Automated Surface Observation System (ASOS) station (RKSS) converted from oktas (eighths of sky) for comparison against the model. The timing of the frontal passages is shown in light blue, and the haze buildup is shown in grey.

References

Atkinson, R., Baulch, D. L., Cox, R. A., Crowley, J. N., Hampson, R. F., Hynes, R. G., Jenkin, M. E., Rossi, M. J., Troe, J., and IUPAC Subcommittee: Evaluated kinetic and photochemical data for atmospheric chemistry: Volume II; gas phase reactions of organic species, Atmos. Chem. Phys., 6, 3625–4055, https://doi.org/10.5194/acp-6-3625-2006, 2006.

Fairall, C. W., Bariteau, L., Grachev, A. A., Hill, R. J., Wolfe, D. E., Brewer, W. A., Tucker, S. C., Hare, J. E., and Angevine, W. M.: Turbulent bulk transfer coefficients and ozone deposition velocity in the International Consortium for Atmospheric Research into Transport and Transformation: COASTAL BULK TRANSFER COEFFICIENTS, J. Geophys. Res., 111, https://doi.org/10.1029/2006JD007597, 2006.

Fairlie, T. D., Jacob, D. J., Dibb, J. E., Alexander, B., Avery, M. A., van Donkelaar, A., and Zhang, L.: Impact of mineral dust on nitrate, sulfate, and ozone in transpacific Asian pollution plumes, Atmos. Chem. Phys., 10, 3999–4012, https://doi.org/10.5194/acp-10-3999-2010, 2010.

Guo, H., Campuzano-Jost, P., Nault, B. A., Day, D. A., Schroder, J. C., Kim, D., Dibb, J. E., Dollner, M., Weinzierl, B., and Jimenez, J. L.: The importance of size ranges in aerosol instrument intercomparisons: a case study for the Atmospheric Tomography Mission, Atmos. Meas. Tech., 14, 3631–3655, doi:10.5194/amt-14-3631-2021, 2021.

Heim, E. W., Dibb, J., Scheuer, E., Jost, P. C., Nault, B. A., Jimenez, J. L., Peterson, D., Knote, C., Fenn, M., Hair, J., Beyersdorf, A. J., Corr, C., and Anderson, B. E.: Asian dust observed during KORUS-AQ facilitates the uptake and incorporation of soluble pollutants during transport to South Korea, Atmos. Env., 117305, https://doi.org/10.1016/j.atmosenv.2020.117305, 2020.

Holmes, C. D., Bertram, T. H., Confer, K. L., Graham, K. A., Ronan, A. C., Wirks, C. K. and Shah, V.: The Role of Clouds in the Tropospheric NOx Cycle: A New Modeling Approach for Cloud Chemistry and Its Global Implications, Geophys. Res. Lett., 46(9), 4980–4990, 2019.

Jenkin, M. E., Saunders, S. M., and Pilling, M. E.: The tropospheric degradation of volatile organic compounds: a protocol for mechanism development, 31, 81–104, 1997.

Jeong, D., Seco, R., Gu, D., Lee, Y., Nault, B. A., Knote, C. J., Mcgee, T., Sullivan, J. T., Jimenez, J. L., Campuzano-Jost, P., Blake, D. R., Sanchez, D., Guenther, A. B., Tanner, D., Huey, L. G., Long, R., Anderson, B. E., Hall, S. R., Ullmann, K., Shin, H., Herndon, S. C., Lee, Y., Kim, D., Ahn, J., and Kim, S.: Integration of airborne and ground observations of nitryl chloride in the Seoul metropolitan area and the implications on regional oxidation capacity during KORUS-AQ 2016, Atmos. Chem. Phys., 19, 12779–12795, https://doi.org/10.5194/acp-19-12779-2019, 2019.

Jordan, C., Crawford, J. H., Beyersdorf, A. J., Eck, T. F., Halliday, H. S., Nault, B. A., Chang, L.-S., Park, J., Park, R., Lee, G., Kim, H., Ahn, J., Cho, S., Shin, H. J., Lee, J. H., Jung, J., Kim, D.-S., Lee, M., Lee, T., Whitehill, A., Szykman, J., Schueneman, M. K., Campuzano-Jost, P., Jimenez, J. L., DiGangi, J. P., Diskin, G. S., Anderson, B. E., Moore, R. H., Ziemba, L. D., Fenn, M. A., Hair, J. W., Kuehn, R. E., Holz, R. E., Chen, G., Travis, K., Shook, M., Peterson, D. A., Lamb, K. D., and Schwarz, J. P.: Investigation of factors controlling $PM_{2.5}$ variability across the South Korean Peninsula during KORUS-AQ, Elementa, 8, 28, https://doi.org/10.1525/elementa.424, 2020.

McNaughton, C. S., Clarke, A. D., Howell, S. G., Pinkerton, M., Anderson, B., Thornhill, L., Hudgins, C., Winstead, E., Dibb, J. E., Scheuer, E., and Maring, H.: Results from the DC-8 Inlet Characterization Experiment (DICE): Airborne Versus Surface Sampling of Mineral Dust and Sea Salt Aerosols, Aerosol Science and Technology, 41, 136–159, https://doi.org/10.1080/02786820601118406, 2007.

Nault, B. A., Campuzano-Jost, P., Day, D. A., Schroder, J. C., Anderson, B., Beyersdorf, A. J., Blake, D. R., Brune, W. H., Choi, Y., Corr, C. A., Gouw, J. A. de, Dibb, J., DiGangi, J. P., Diskin, G. S., Fried, A., Huey, L. G., Kim, M. J., Knote, C. J., Lamb, K. D., Lee, T., Park, T., Pusede, S. E., Scheuer, E., Thornhill, K. L., Woo, J.-H., and Jimenez, J. L.: Secondary organic aerosol production from local emissions dominates the organic aerosol budget over Seoul, South Korea, during KORUS-AQ, Atmos. Chem. Phys., 18, 17769–17800, https://doi.org/10.5194/acp-18-17769-2018, 2018.

Neuman, J. A., Parrish, D. D., Ryerson, T. B., Brock, C. A., Wiedinmyer, C., Frost, G. J., Holloway, J. S., and Fehsenfeld, F. C.: Nitric acid loss rates measured in power plant plumes: NITRIC ACID LOSS RATES, J. Geophys. Res., 109, https://doi.org/10.1029/2004JD005092, 2004.

Parrish, D. D., Stohl, A., Forster, C., Atlas, E. L., Blake, D. R., Goldan, P. D., Kuster, W. C., and de Gouw, J. A.: Effects of mixing on evolution of hydrocarbon ratios in the troposphere: MIXING EFFECTS ON NMHC RATIO EVOLUTION, J. Geophys. Res., 112, https://doi.org/10.1029/2006JD007583, 2007.

Perring, A. E., Bertram, T. H., Farmer, D. K., Wooldridge, P. J., Dibb, J., Blake, N. J., Blake, D. R., Singh, H. B., Fuelberg, H., Diskin, G., Sachse, G., and Cohen, R. C.: The production and persistence of RONO2 in the Mexico City plume, Atmos. Chem. Phys., 10, 7215–7229, https://doi.org/10.5194/acp-10-7215-2010, 2010.

Qiu, X., Ying, Q., Wang, S., Duan, L., Zhao, J., Xing, J., Ding, D., Sun, Y., Liu, B., Shi, A., Yan, X., Xu, Q., and Hao, J.: Modeling the impact of heterogeneous reactions of chlorine on summertime nitrate formation in Beijing, China, Atmos. Chem. Phys., 19, 6737–6747, https://doi.org/10.5194/acp-19-6737-2019, 2019.

Li, X. and Rappenglueck, B.: A study of model nighttime ozone bias in air quality modeling, Atmos. Environ., 19, 2018.

Sarwar, G., Simon, H., Bhave, P., and Yarwood, G.: Examining the impact of heterogeneous nitryl chloride production on air quality across the United States, Atmos. Chem. Phys., 12, 6455–6473, https://doi.org/10.5194/acp-12-6455-2012, 2012.

Saunders, S. M., Jenkin, M. E., Derwent, R. G., and Pilling, M. J.: Protocol for the development of the Master Chemical Mechanism, MCM v3 (Part A): tropospheric degradation of non-aromatic volatile organic compounds, 20, 2003.

Schlosser, J., Stahl, C., Sorooshian, A., Le, Y. T.-H., Jeon, K.-J., Xian, P., Jordan, C. E., Travis, K. R., Crawford, J. H., Gong, S. Y., Shin, H.-J., Song, I.-H., and Youn, J.: Evidence of haze-driven secondary production of supermicrometer aerosol nitrate and sulfate in size distribution data in South Korea, Aerosols/Field Measurements/Troposphere/Chemistry (chemical composition and reactions), https://doi.org/10.5194/acp-2021-1098, 2022.

Simpson, I. J., Blake, D. R., Blake, N. J., Meinardi, S., Barletta, B., Hughes, S. C., Fleming, L. T., Crawford, J. H., Diskin, G. S., Emmons, L. K., Fried, A., Guo, H., Peterson, D. A., Wisthaler, A., Woo, J.-H., Barré, J., Gaubert, B., Kim, J., Kim, M. J., Kim, Y., Knote, C., Mikoviny, T., Pusede, S. E., Schroeder, J. R., Wang, Y., Wennberg, P. O., and Zeng, L.: Characterization, sources and reactivity of volatile organic compounds (VOCs) in Seoul and surrounding regions during KORUS-AQ, Elementa, 8, 37, https://doi.org/10.1525/elementa.434, 2020.

Sun, Y., He, Y., Kuang, Y., Xu, W., Song, S., Ma, N., Tao, J., Cheng, P., Wu, C., Su, H., Cheng, Y., Xie, C., Chen, C., Lei, L., Qiu, Y., Fu, P., Croteau, P. and Worsnop, D. R.: Chemical differences between PM_1 and $PM_{2.5}$ in highly polluted environment and implications in air pollution studies, Geophys. Res. Lett., 47(5), doi:10.1029/2019gl086288, 2020.

Teng, A. P., Crounse, J. D., Lee, L., St. Clair, J. M., Cohen, R. C., and Wennberg, P. O.: Hydroxy nitrate production in the OH-initiated oxidation of alkenes, Atmos. Chem. Phys., 15, 4297–4316, https://doi.org/10.5194/acp-15-4297-2015, 2015.

Wang, X., Jacob, D. J., Eastham, S. D., Sulprizio, M. P., Zhu, L., Chen, Q., Alexander, B., Sherwen, T., Evans, M. J., Lee, B. H., Haskins, J. D., Lopez-Hilfiker, F. D., Thornton, J. A., Huey, G. L., and Liao, H.: The role of chlorine in global tropospheric chemistry, Atmos. Chem. Phys., 19, 3981–4003, https://doi.org/10.5194/acp-19-3981-2019, 2019.

Wang, X., Jacob, D. J., Fu, X., Wang, T., Breton, M. L., Hallquist, M., Liu, Z., McDuffie, E. E., and Liao, H.: Effects of Anthropogenic Chlorine on $PM_{2.5}$ and Ozone Air Quality in China, Environ. Sci. Technol., 54, 9908–9916, https://doi.org/10.1021/acs.est.0c02296, 2020.

Wang, X., Jacob, D. J., Downs, W., Zhai, S., Zhu, L., Shah, V., Holmes, C. D., Sherwen, T., Alexander, B., Evans, M. J., Eastham, S. D., Neuman, J. A., Veres, P., Koenig, T. K., Volkamer, R., Huey, L. G., Bannan, T. J., Percival, C. J., Lee, B. H., and Thornton, J. A.: Global tropospheric halogen (Cl, Br, I) chemistry and its impact on oxidants, Atmos. Chem. Phys., https://doi.org/10.5194/acp-2021-441, 2021.

Zhai, S., Jacob, D. J., Brewer, J. F., Li, K., Moch, J. M., Kim, J., Lee, S., Lim, H., Lee, H. C., Kuk, S. K., Park, R. J., Jeong, J. I., Wang, X., Liu, P., Luo, G., Yu, F., Meng, J., Martin, R. V., Travis, K. R., Hair, J. W., Anderson, B. E., Dibb, J. E., Jimenez, J. L., Campuzano-Jost, P., Nault, B. A., Woo, J.-H., Kim, Y., Zhang, Q., and Liao, H.: Interpretation of geostationary satellite aerosol optical depth (AOD) over East Asia in relation to fine particulate matter ($PM_{2.5}$): insights from the KORUS-AQ aircraft campaign and seasonality, Atmos. Chem. Phys., https://doi.org/10.5194/acp-2021-413, 2021.